





Cite this: *Mater. Adv.*, 2021,  
2, 455

# Efficient electrochemical water splitting using copper molybdenum sulfide anchored Ni foam as a high-performance bifunctional catalyst†

Aparna Sajeev, <sup>a</sup> Vimal Kumar Mariappan, <sup>a</sup> Dhanasekar Kesavan,<sup>a</sup>  
Karthikeyan Krishnamoorthy <sup>a</sup> and Sang-Jae Kim <sup>\*ab</sup>

The necessity of developing a bifunctional catalyst for the hydrogen evolution reaction (HER) and oxygen evolution reaction (OER) has increased due to the urge to meet the future renewable energy requirements. This work demonstrated the use of copper molybdenum sulfide nanostructures on Ni foam (CMS/Ni) as a bifunctional catalyst for the HER and OER. Physicochemical characterizations such as X-ray diffraction, X-ray photoelectron spectroscopy, and field-emission scanning electron microscopic analyses confirmed the formation of hierarchical CMS nanostructures on Ni foam using a hydrothermal method. The CMS/Ni electrocatalyst exhibits excellent electrocatalytic properties in an alkaline electrolyte (1 M KOH) with a low overpotential of about 213 and 350 mV for the HER and OER (to drive a current density of 50 mA cm<sup>-2</sup>) and Tafel slope values of 80 and 124 mV dec<sup>-1</sup>, respectively. A lab-scale water electrolyzer is constructed using the CMS/Ni electrocatalyst (as anode and cathode), which requires a low voltage of 1.62 V (at a current density of 50 mA cm<sup>-2</sup>) for electrochemical water splitting reaction. The multi-current and long-term stability analysis suggested better electrocatalytic properties of the CMS/Ni electrode. Finally, a self-powered water electrolyzer system was constructed via integration of a solar cell with the fabricated CMS/Ni electrolyzer, which demonstrated potential application towards next-generation energy conversion and management systems.

Received 8th September 2020,  
Accepted 28th November 2020

DOI: 10.1039/d0ma00688b

rsc.li/materials-advances

## 1. Introduction

The development of sustainable green energy technologies is expected to replace the endangered traditional energy resources that cause major global pollution issues in the world.<sup>1,2</sup> Therefore, the development of sustainable energy devices such as fuel cells, metal-air batteries, electrocatalytic and photocatalytic conversion techniques is focused on solving the overall energy crisis.<sup>3–8</sup> Electrochemical water splitting is a promising energy process that can produce zero-carbon emission hydrogen gas *via* electrocatalytic energy conversion. Furthermore, it has more benefits than using the power from wind and solar energy for cost-effective production.<sup>2,9–11</sup> The principle of electrochemical water splitting occurs *via* the hydrogen evolution reaction (HER) at the cathode and oxygen evolution reaction (OER) at the anode.<sup>5</sup> The choice of electrocatalytic materials significantly impacts the

device performance (low overpotentials) to reach the level of widely used HER (platinum-based) and OER catalysts (iridium/ruthenium-based).<sup>12,13</sup> The high cost of these noble metals limits their wide practical applications, especially in the development of large-scale manufacturing.<sup>14</sup> This results in huge demand to develop low-cost, noble metal-free catalysts with high electrocatalytic properties.

In this context, developing a bifunctional catalyst capable of driving both HER and OER reactions is of great interest in reducing the overall manufacturing cost and preventing cross-contamination during a long cycle.<sup>15</sup> Currently, transition metal-based chalcogenides, phosphides, oxides, and their derivatives are being examined as bifunctional catalysts in an alkaline medium.<sup>2,16–21</sup> However, these materials still need to be further engineered to reduce the overpotentials in both the anode and cathode during the electrochemical water splitting reactions.<sup>22</sup> It is expected that multicomponent transition metal-based catalysts can be an ideal candidate for electrocatalytic reactions due to their high redox states and improved conductivity over their single component ones.<sup>23,24</sup> For instance, 2D MoS<sub>2</sub> nanosheets are examined as promising HER catalysts in the water-splitting reactions due to their ability to chemisorb hydrogen (in both acidic and alkaline

<sup>a</sup> Nanomaterials & System Laboratory, Major of Mechatronics Engineering, Faculty of Applied Energy System, Jeju National University, Jeju 63243, Republic of Korea. E-mail: kimsangj@jeju.ac.kr

<sup>b</sup> Department of Advanced Convergence Science & Technology, Jeju National University, Jeju-63243, South Korea

† Electronic supplementary information (ESI) available. See DOI: 10.1039/d0ma00688b

environment) *via* the S-edge sites in the 2D lattice.<sup>10</sup> However, these materials are proven to be a poor OER catalyst, which was tailored *via* incorporation of a transition metal or nanohybrids decoration to enhance the OER. Recently, Zhu *et al.* demonstrated this synergistic effect approach through preparing a Co<sub>9</sub>S<sub>8</sub>/MoS<sub>2</sub> composite, which established a higher catalytic activity than their individual performances because of the increased charge transfer between the Mo and Co atoms through S-linkage.<sup>25</sup> Wang *et al.* reported a CoNi<sub>2</sub>S<sub>4</sub> electrocatalyst synthesized through a one pot hydrothermal method that shows an electrochemical activity of HER with a Tafel slope value of 85 mV dec<sup>-1</sup> with an overpotential of 255 mV at 10 mA cm<sup>-2</sup>.<sup>26</sup> Shichun *et al.* reported that a Mo-N/C@MoS<sub>2</sub> electrocatalyst showed an electrochemical OER activity which required an overpotential of 390 mV to attain a current density of 10 mA cm<sup>-2</sup>.<sup>27</sup> In the view of lowering the overpotential values of the HER/OER and reducing the required voltage for water splitting reactions in full devices, it is strongly required to develop novel bifunctional catalysts.

In these regards, copper molybdenum sulfide (Cu<sub>2</sub>MoS<sub>4</sub>, CMS) from the family of Cu<sub>2</sub>MX<sub>4</sub> is more attractive due to its intrinsic physical and chemical properties with rich electrochemistry.<sup>7,28</sup> CMS nanostructures prepared *via* different chemical methods have been explored as an excellent photocatalytic (due to wide bandgap),<sup>29</sup> HER,<sup>30</sup> and pseudocapacitive material.<sup>31</sup> Our recent studies have demonstrated the exceptional capacitive nature of the CMS nanostructures in 1 M Na<sub>2</sub>SO<sub>4</sub> electrolyte with a specific capacitance of 265.62 F g<sup>-1</sup>.<sup>32</sup> Even though CMS powders were experimentally demonstrated as a HER catalyst, their performance as a catalyst for the OER and effectiveness in overall electrochemical water splitting is not yet studied. In this work, we have demonstrated the use of hierarchical CMS nanostructures grown on Ni foam as a novel bifunctional catalyst for water splitting applications. Furthermore, we also presented a self-powered system *via* integration of a solar power station to drive the CMS water electrolyzer as a proof of concept.

## 2. Experimental section

### 2.1 Materials

Copper(II) sulfate pentahydrate (CuSO<sub>4</sub>·5H<sub>2</sub>O), sodium molybdate (Na<sub>2</sub>MoO<sub>4</sub>), thioacetamide (CH<sub>3</sub>CSNH<sub>2</sub>), sodium sulfate (Na<sub>2</sub>SO<sub>4</sub>), copper(II) oxide (CuO), and ethylene glycol (C<sub>2</sub>H<sub>6</sub>O<sub>2</sub>) were procured from Daejung Chemicals Ltd, South Korea. The nickel (Ni) foam (thickness 1.7 mm) was purchased from Heze Jiao tong Xinda Import and Export Co., Ltd. Prior to the hydrothermal process, Ni foam was pre-cleaned with diluted HCl followed by acetone, and deionized (DI) water *via* a sonication process to remove the presence of dust and native surface oxide layer.<sup>33</sup>

### 2.2 Growth of copper molybdenum sulfide nanostructures on Ni foam

A hydrothermal method was used to grow the copper molybdenum sulfide (CMS) nanostructures on the porous Ni foam using the same procedure reported in our previous work.<sup>32</sup> Briefly,

Na<sub>2</sub>MoO<sub>4</sub> and CH<sub>3</sub>CSNH<sub>2</sub> in the weight ratio of 1:2 were dissolved in 60 mL of ethylene glycol under an ultrasonication process for 1 h. This process led to the formation of a light-yellowish, green-colored solution ensuring the complete dissolution of Na<sub>2</sub>MoO<sub>4</sub> and CH<sub>3</sub>CSNH<sub>2</sub> in C<sub>2</sub>H<sub>6</sub>O<sub>2</sub>. Subsequently, 40 mg of CuO was added slowly to the above solution and ultrasonicated until the color of the solution turned dark brown. The prepared precursor solution was later transferred to a Teflon lined stainless steel autoclave (100 mL) in which the precleaned Ni-foam was immersed. The hydrothermal reaction was carried out by placing the autoclave in a hot air oven for 15 h at 150 °C and then naturally allowed to cool down to room temperature. Hereafter, the settled black colored CMS powders on the bottom of the vessel and CMS/Ni foam substrate were carefully washed using water and ethanol to remove the impurities. Finally, the CMS powders and CMS/Ni foam samples were dried in an oven at 60 °C for 12 h.

### 2.3 Instrumentation

The phase and crystallinity of the CMS/Ni electrode were determined using an X-ray diffractometer system (Empyrean) with Cu-K $\alpha$  radiation ( $\lambda$  = 1.5418 Å). The analysis of the elements chemical state in the CMS/Ni foam was done using an X-ray photoelectron spectrometer (ESCA-2000, VG Microtech Ltd). The surface morphology and elemental mapping analysis were scrutinized with field-emission scanning electron microscopy (TESCAN, MIRA3) under various magnifications using an energy dispersive X-ray (EDS) spectroscopy and a transmission emission scanning electron microscope (HR-TEM, JEOL JEM 2011, JEOL Ltd).

### 2.4 Electrochemical measurements

All of the electrochemical measurements were carried on Autolab PGSTAT302N electrochemical workstation. The individual electrode properties of the CMS/Ni electrode for the HER and OER were accessed using a three-electrode configuration test by employing the working electrode (CMS/Ni), reference electrode (Ag/AgCl), and counter electrode (platinum sheet) respectively. The electrochemical measurements such as linear sweep voltammetry (LSV) were performed using 1 M KOH aqueous electrolyte at a scan rate of 10 mV s<sup>-1</sup>. The potential values provided in the LSV polarization curves were iR-corrected unless specifically indicated, and the potential values were reported with respect to RHE (converted from the Ag/AgCl scale using a calibration). The electrochemical active surface area of the CMS/Ni electrocatalyst was determined using the ratio of double-layer capacitance ( $C_{dl}$ ) to that of the specific capacitance as reported in the literature.<sup>34–36</sup> The double-layer capacitance ( $C_{dl}$ ) was estimated from the non-faradaic region through CVs recorded at different scan rates. The overall water splitting experiments were performed using a two-electrode configuration system, using two symmetric CMS/Ni foam as the cathode and anode, respectively. Furthermore, the practical applicability of the CMS/Ni water electrolyzer was demonstrated by utilizing three solar panels (connected in parallel)



as a sustainable power source to drive the water electrolyzer for hydrogen production.

### 3. Results and discussion

The copper molybdenum sulfide nanostructures were grown on the surface of Ni foam *via* a one-step hydrothermal route as reported in our earlier work,<sup>32</sup> and the product is denoted as the CMS/Ni electrode. The X-ray diffraction (XRD) pattern of the CMS/Ni electrode shows that the diffraction peaks correspond to the bare Ni foam (Fig. 1(A)), and tetragonal Cu<sub>2</sub>MoS<sub>4</sub> (Fig. 1(B)). There are no peaks related to any other form of single component sulfides detected in the XRD pattern, which suggested the formation of CMS/Ni foam. Fig. 1(C) exhibits the XPS survey spectrum of the CMS/Ni foam, indicating the presence of elements such as Mo 3d, Cu 2p, S 2p, and Ni 2p, with C 1s and O 1s. The core-level spectrum of the Cu 2p states (Fig. 1(D)) exhibited the existence of the two prominent peaks at 953.15 eV (Cu 2p<sub>1/2</sub>) and 933.10 eV (Cu 2p<sub>3/2</sub>) with a peak separation of 20.05 eV suggesting that the oxidation state of Cu in CMS/Ni is about +1. The deconvoluted spectrum of the Mo 3d states (Fig. 1(E)) shows the presence of peaks due to Mo<sup>4+</sup> 3d<sub>5/2</sub> (228.75 eV), Mo<sup>4+</sup> 3d<sub>3/2</sub> (232.63 eV), Mo<sup>6+</sup> 3d<sub>5/2</sub> (231.89 eV), and Mo<sup>6+</sup> 3d<sub>3/2</sub> (235.16 eV) and with an additional peak at 226.16 eV (S 2s), respectively.<sup>37</sup> Fig. 1(F) shows the core-level spectrum of the S 2p state, presenting two peaks at 162.2 and 168.58 eV that correspond to S 2p<sub>3/2</sub> and their satellites, suggesting that the oxidation state of S 2p in the CMS/Ni is

found to be −2. Fig. S1, ESI† describes the core level spectrum of the Ni 2p states present in the CMS/Ni. Fig. 2 summarizes the morphological and elemental analysis of the CMS/Ni foam. The field emission scanning electron microscopic (FE-SEM) image given in Fig. 2(A–C) with different levels of magnification suggested the uniform growth of CMS nanostructures (with size in the range from 100 to 200 nm) on the surface of the Ni foam. Fig. 2(D) shows the micrograph used for elemental analysis to identify the elements (Ni, Cu, Mo and S) present in CMS/Ni foam as given in Fig. 2(E–H). The EDS spectrum given in Fig. 2(I) further confirms the presence of Cu, Mo and S elements in the prepared CMS/Ni foam. The high-resolution transmission electron micrographs (HR-TEM) of the CMS nanostructures (peeled off from the CMS/Ni) recorded under various magnifications are provided in Fig. 3(A–C). This showed that the size of the CMS nanostructures lies in the range of 50 to 100 nm, respectively. The corresponding elemental maps of CMS nanostructures given in Fig. 3(D–F) highlight the homogeneous distribution of Cu, Mo, and S elements present in the prepared CMS.

Fig. 4 shows the HER properties of the CMS/Ni foam compared with bare Ni foam using an aqueous electrolyte of 1 M KOH at room temperature. Fig. 4(A) depicts the LSV polarization curve of bare Ni and CMS/Ni foam for the HER, which shows the low onset potential (−0.18 V vs. RHE) of the CMS/Ni electrocatalyst compared to that of the bare Ni electrode. The porous CMS/Ni electrocatalyst attains a HER current density of 50 mA cm<sup>−2</sup> at an overpotential ( $\eta_{50}$ ) of 213 mV, which is lower compared to the bare Ni foam electrodes with an

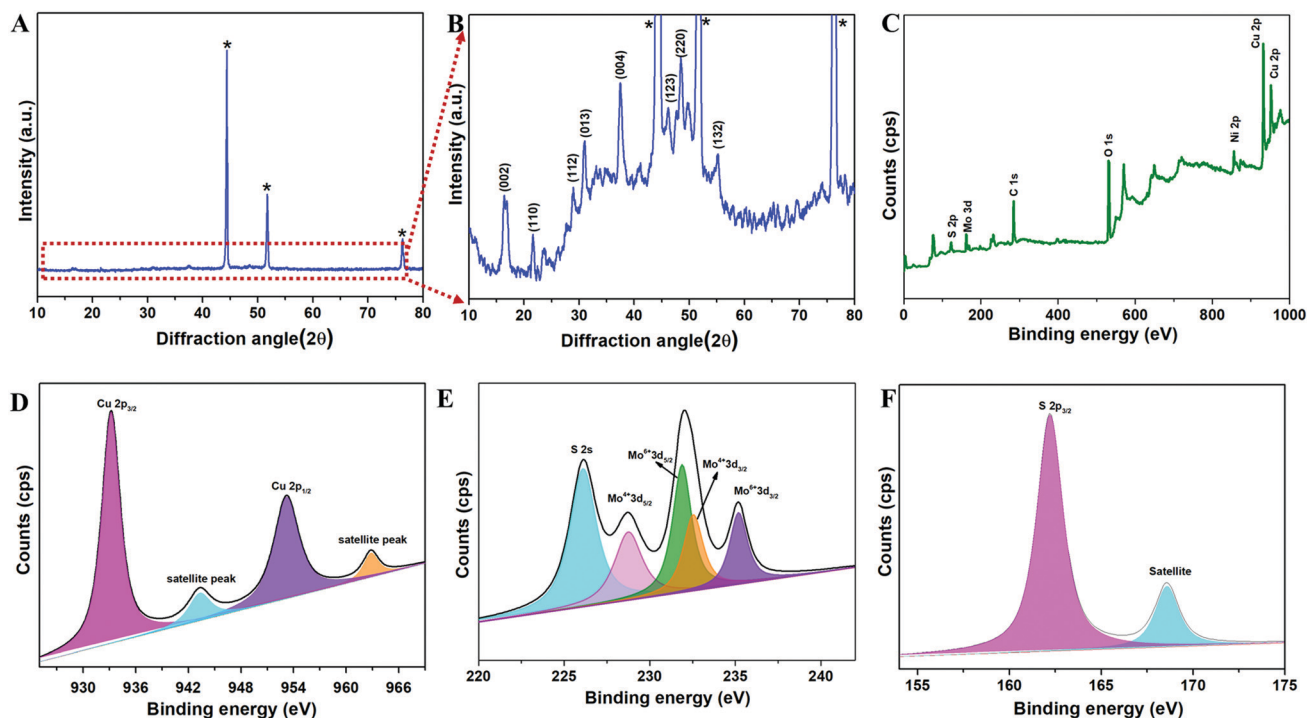


Fig. 1 Physicochemical characterization of CMS/Ni foam. (A and B) X-ray diffraction pattern of CMS on Ni foam; (C) XPS survey spectrum of CMS/Ni foam; (D) core-level spectrum of the Cu 2p state; (E) core-level spectrum of the Mo 3d state; (F) core-level spectrum of the S 2p state, respectively.



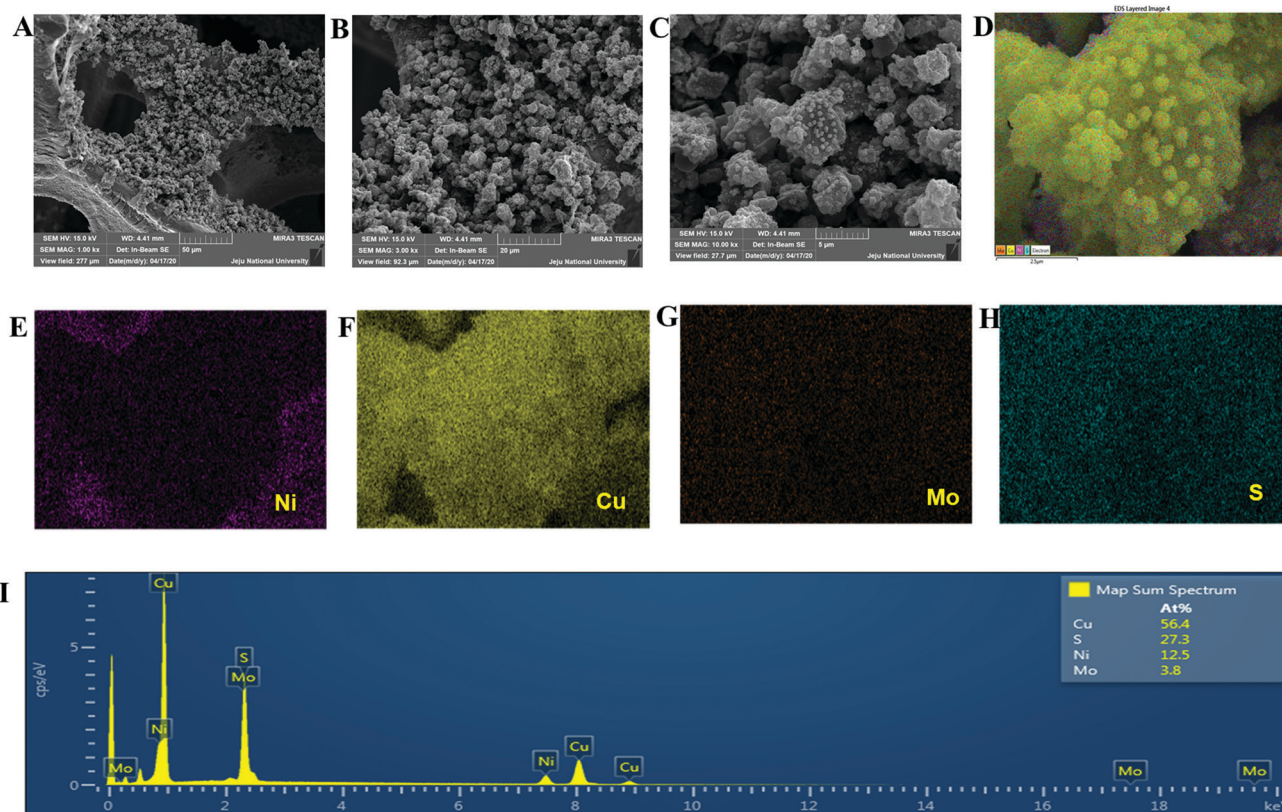


Fig. 2 Morphological characterization of CMS/Ni foam. (A–C) Field emission-scanning electron micrograph of CMS/Ni foam at different magnifications; elemental mapping analysis of CMS/Ni foam (D) overlay field emission scanning micrograph; (E) Ni; (F) Cu; (G) Mo; (H) S and (I) EDX spectrum of CMS/Ni foam.

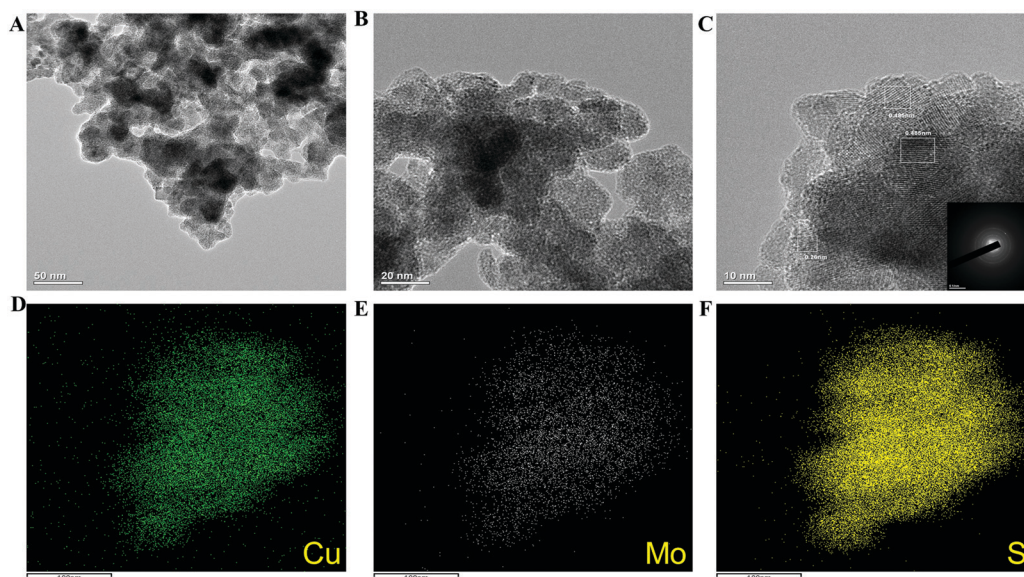


Fig. 3 (A–C) High-resolution transmission electron micrographs of CMS nanostructures and (D–F) elemental maps of Cu, Mo, and S present in the CMS.

overpotential of 283 mV. The HER performance of the CMS/Ni foam electrocatalyst is better compared to the recently reported electrocatalysts such as  $\text{NiCo}_2\text{S}_4$  NW/NF ( $\eta_{10} = 210$  mV),  $\text{CoS}_x/\text{Ni}_3\text{S}_2$ @NF NF ( $\eta_{10} = 240$  mV),  $\text{Ni-Co-S}$  ( $\eta_{10} = 280$  mV), and others given in Table S1, ESI.†<sup>38–40</sup> Fig. 4(B) shows the Tafel

plots obtained over the region from 50 to 100  $\text{mA cm}^{-2}$ , which showed Tafel slope values of 80  $\text{mV dec}^{-1}$  smaller than  $\text{CoS}_x/\text{Ni}_3\text{S}_2$ @NF (133.32  $\text{mV dec}^{-1}$ ),  $\text{Co}_9\text{S}_8$  HNSs (111  $\text{mV dec}^{-1}$ ), and so on.<sup>39,41</sup> The Tafel slope value is calculated to analyze the possible HER kinetics of the CMS/Ni electrocatalyst, as



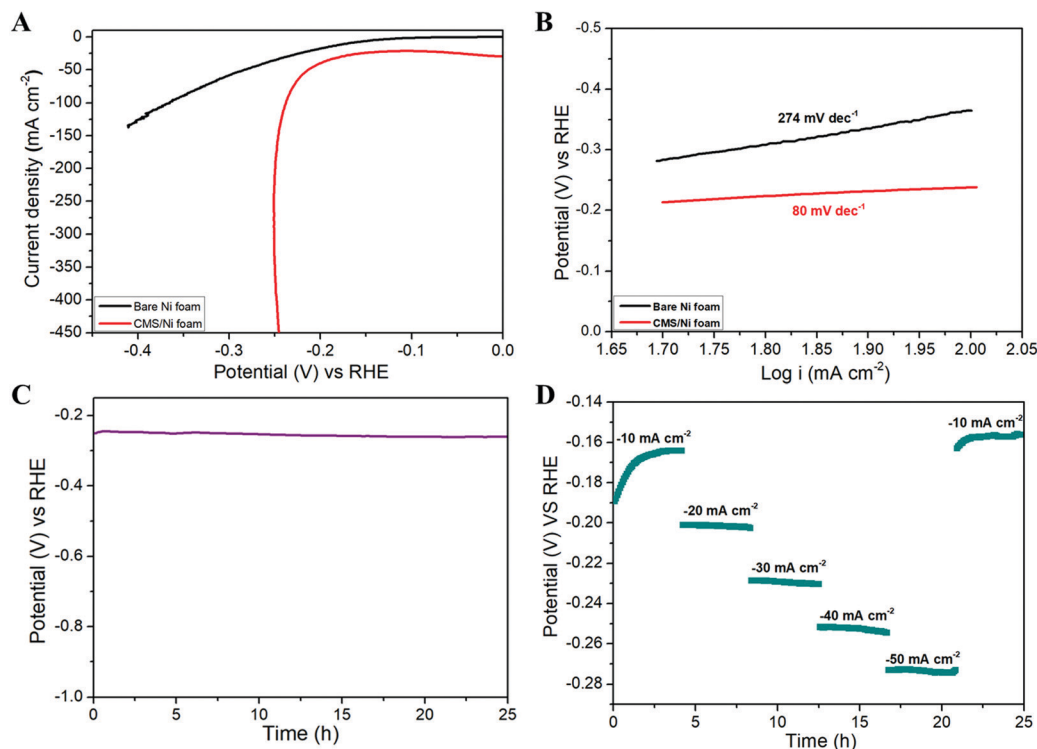


Fig. 4 Electrochemical characterization of CMS/Ni for HER analysis in 1 M KOH. (A) LSV curves (iR-compensated) of CMS/Ni foam and bare Ni foam (scan rate of 10 mV s<sup>-1</sup>), (B) Tafel plots, (C) chronopotentiometry durability test (without iR-compensated) at a constant current density of -50 mA cm<sup>-2</sup>, (D) chronopotentiometry durability test with different applied currents, respectively.

shown in Fig. 4(B). The Tafel slope of 80 mV dec<sup>-1</sup> was found for the CMS/Ni electrocatalyst, whereas it is about 274 mV dec<sup>-1</sup> for the bare Ni electrode. The CMS/Ni electrocatalyst shows a very low Tafel slope value compared with Ni foam, which indicated that the former possesses a hassle-free HER kinetics. Fig. 4(C) shows the long-term stability of the CMS/Ni electrocatalyst analyzed using chronopotentiometry (at 50 mA cm<sup>-2</sup>) for 25 h. It showed a potential of -0.250 V initially, which increased up to -0.260 V after continuous reaction and is stable until 25 h, which suggested the electrochemical stability of the CMS/Ni electrocatalyst. The observed small increase in the potential values during the initial cycles might be due to the electro-activation effect as a cause of the wettability of the CMS/Ni electrocatalyst. Fig. S2, ESI† shows the HER polarization curves of the CMS/Ni electrocatalyst before and after stability tests, which shows an increase in overpotential value from 213 to 229 mV. This small shift in overpotential value is a reasonable one which also affirms their better electrochemical stability. Fig. 4(D) shows the HER multi-current analysis of the CMS/Ni electrocatalyst over 25 h analyzed using the chronopotentiometry method (using different applied current densities ranging from -10 to -50 mA cm<sup>-2</sup>). It showed that the measured potential values were recovered after ramping with different levels of applied current ranges after 25 h. These measurements indicated the use of the CMS/Ni electrocatalyst as a promising candidate for HER applications.

Fig. 5 shows the OER properties of the CMS/Ni foam in comparison with bare Ni foam using an aqueous electrolyte of 1 M KOH at room temperature. Fig. 5(A) depicts the LSV

polarization curve of bare Ni and CMS/Ni foam for the OER, which shows the lower onset potential (1.5 V vs. RHE) of the CMS/Ni electrocatalyst than that of the bare Ni electrode. This suggested that the improved OER catalytic properties of the Ni electrode after the growth of CMS nanostructures on their surface. In Fig. 5(A), an intense oxidation peak was identified at ~1.43 V vs. RHE as a result of Ni(II)-Ni(III) conversion within the electrochemical process.<sup>42</sup> Due to this reaction, the oxygen evolution overpotential ( $\eta$ ) measurement at 10 mA cm<sup>-2</sup> cannot be calculated accurately. Therefore, we have reported the overpotential at a higher current density (50 mA cm<sup>-2</sup>) widely practiced for binder-free electrodes. The porous CMS/Ni electrocatalyst attains OER current density of 50 mA cm<sup>-2</sup> at an overpotential ( $\eta_{50}$ ) of 350 mV, lower than the bare Ni foam electrodes with an overpotential of 570 mV. The obtained overpotential value of the CMS/Ni electrocatalyst ( $\eta_{50}$  = 350 mV) is better than that of the reported electrocatalysts such as CuS ( $\eta_{10}$  = 400 mV), Cu<sub>2</sub>S-Ni<sub>3</sub>S<sub>2</sub>/NF ( $\eta_{10}$  = 329 mV), MoS<sub>2</sub>@CoO ( $\eta_{10}$  = 325 mV), respectively.<sup>43-45</sup> The Tafel slope value is calculated further to analyze the possible OER kinetics of the CMS/Ni electrocatalyst, as shown in Fig. 5(B). The Tafel slope of 124 mV dec<sup>-1</sup> was found for the CMS/Ni electrocatalyst, whereas it is about 237 mV dec<sup>-1</sup> for the bare Ni electrode. The CMS/Ni electrocatalyst shows a very low Tafel slope compared with Ni foam and other recently reported TMO and TMCs (as seen in Table S2, ESI†), which indicated that the former possesses a hassle-free OER kinetics. These values suggested that the OER reaction that occurred at the surface of

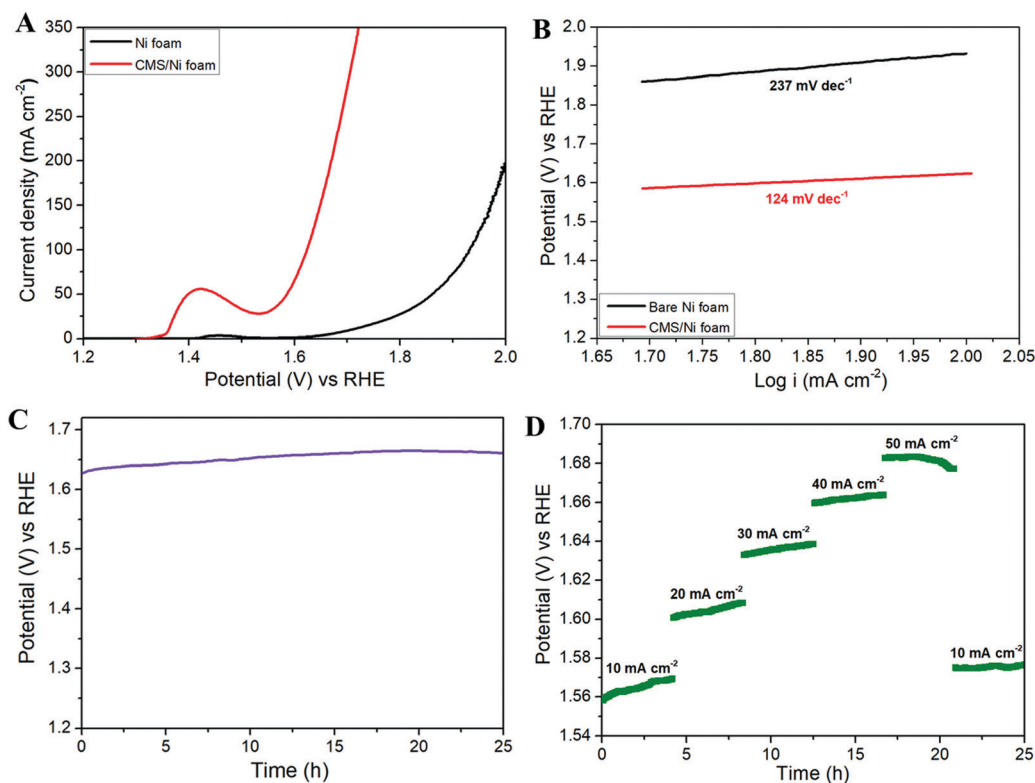


Fig. 5 Electrochemical characterization of CMS/Ni for OER analysis in 1 M KOH. (A) LSV curves (iR-compensated) of CMS/Ni foam and bare Ni foam (scan rate of  $10 \text{ mV s}^{-1}$ ), (B) Tafel plots, (C) chronopotentiometry durability test (without iR-compensation) at a constant current of  $50 \text{ mA cm}^{-2}$ , and (D) chronopotentiometry durability test with different applied currents, respectively.

the CMS/Ni electrode was governed by a one-electron transfer process in accordance with the critical assessment of the electrochemical water splitting reaction suggested by S. Kundu *et al.*<sup>46</sup> Fig. 5(C) shows the long-term stability of the CMS/Ni electrocatalyst analyzed using chronopotentiometry (at  $50 \text{ mA cm}^{-2}$ ) for 25 h. It showed that a potential of 1.62 V was observed initially, which was increased up to 1.66 V after continuous reaction and is stable until 25 h, which suggested the electrochemical stability of the CMS/Ni electrocatalyst. The observed small increase in the potential values during the initial cycles might be due to the electro-activation effect due to the wettability of the CMS/Ni electrocatalyst. Fig. S3, ESI† shows the OER polarization curves of the CMS/Ni electrocatalyst before and after stability tests, which shows an increase in the overpotential values from 350 to 380 mV. This small shift in overpotential values is a reasonable one, which also affirms their better electrochemical stability. Fig. 5(D) shows the OER multi-current analysis of the CMS/Ni electrocatalyst over 25 h as analyzed using the chronopotentiometry method (using different applied current densities ranging from 10 to  $50 \text{ mA cm}^{-2}$ ). This showed that the measured potential values were recovered after ramping with different levels of applied current range after 25 h. These measurements indicated the use of the CMS/Ni electrocatalyst as a promising candidate for OER applications. Electrochemical impedance spectroscopy is a critical analysis to understand the mechanism of charge and ionic transport in an electrochemical system.<sup>47</sup> Fig. S4, ESI†

depicts the Nyquist plot of the CMS/Ni electrocatalyst, which revealed the presence of quasi semi-circles at a high frequency (due to charge transfer resistance) followed by a straight line (Warburg impedance) at the low-frequency regime. The solution resistance ( $R_s$ ) and quasi charge-transfer resistance ( $R_{ct}$ ) of the CMS/Ni electrode are found to be  $0.85 \Omega$  and  $1.4 \Omega$ , which confirms the better conductivity of the prepared CMS/Ni electrode. To determine the electrochemically active surface area (ECSA) of the CMS/Ni electrode, the cyclic voltammograms (CV) of the CMS/Ni electrocatalyst were recorded over the potential from 0.575 to 0.875 V (as given in Fig. S5(A), ESI†) which shows a typical capacitive nature. The anodic and cathodic peak current shows a linear increase in the current ranges in accordance with an increase in the scan rate as seen from Fig. S5(B), ESI† from which the double-layer capacitance ( $C_{dl}$ ) of the CMS/Ni electrode is determined as  $4.45 \text{ mF}$  with a corresponding ECSA of  $111.25 \text{ cm}^2$ .

The above studies suggested the HER and OER properties of the prepared CMS/Ni electrodes tested using the half-cell configuration. However, it is also essential to examine the properties of the CMS/Ni electrocatalyst using full-cell configuration to examine their device specific properties for electrochemical water splitting reactions. Therefore, we have fabricated the CMS/Ni electrode-based lab-scale water electrolyzer (beaker type cell) using two identical CMS/Ni electrodes. Fig. 6(A) shows the LSV polarization curve of a non-precious CMS/Ni electrode-based alkaline water electrolyzer. This indicates





that the CMS/Ni water electrolyzer requires a minimum voltage of 1.62 V to attain  $10 \text{ mA cm}^{-2}$ , which is a benchmark current value for practical applications. The obtained voltage values for the CMS/Ni water electrolyzer are comparable to that of the precious electrocatalyst and lower compared to the other recently reported bifunctional electrocatalysts such as  $\text{CoNi}_2\text{S}_4/\text{Ni}_3\text{S}_2@\text{NF}$  (1.65 V),  $\text{Co}_9\text{S}_8/\text{Ni}_3\text{S}_2$  (1.64 V),  $\text{Co}_9\text{S}_8@\text{MoS}_2$  (1.67 V),  $\text{NiCo}_2\text{S}_4$  NA/CC (1.68 V) and others listed in Table S3 (ESI†).<sup>48–50</sup> The excellent electrochemical performance of the CMS/Ni electrocatalyst for the HER and OER is ascribed to several factors: (i) the presence of hierarchical nanostructures,<sup>38</sup> (ii) the elimination of the insulating binder,<sup>33</sup> (iii) direct integration of the CMS nanostructures on Ni foam resulting in efficient electron transfer kinetics,<sup>42</sup> and (iv) the improved electrical conductivity and electrochemical reactivity of CMS nanostructures.<sup>51</sup>

Fig. 6(B) shows the long-term durability test of the fabricated CMS/Ni water electrolyzer, which shows that the voltage value varies from 1.75 to 1.71 V ( $10 \text{ mA cm}^{-2}$ ), suggesting their superior stability. The multi-current analysis of the fabricated CMS/Ni water electrolyzer (shown in Fig. 6(C)) shows that the voltage values are changed with respect to the applied current ranges and recovered back. Fig. 6(D) shows the LSV profiles of the CMS/Ni water electrolyzer, which shows only a small noticeable change in the over-potential values even after 50 h of continuous operation. To analyze the structural stability of the CMS/Ni electrode, we have performed their XRD and FE-SEM analysis after a long-term stability test. Fig. S6(A) (ESI†) shows the XRD pattern of

the CMS/Ni electrode before and after electrochemical stability (after 25 h). It showed significant differences as follows: The characteristic diffraction peak of the CMS nanostructure at  $16.1^\circ$  (corresponding to the (002) plane of CMS) becomes broadened as a result of long-term ion intercalation into the layered sites of the CMS nanostructures. Fig. S6(B–D), ESI† confirms that there is no significant change in the morphology of the CMS/Ni electrode after electrochemical stability tests and it also highlights the good adherence of the CMS on the Ni foam. The EDX spectrum shown in Fig. S6(E), ESI† shows the presence of K and O elements due to the use of KOH electrolyte in addition to the C, Mo, S, and Ni elements present in CMS/Ni. Fig. S6(F–L), ESI† confirms the presence of potassium and oxygen from KOH on the surface of the CMS/Ni electrode. The XRD, FE-SEM and elemental mapping indicated that the CMS/Ni foam possesses good structural stability, which is an important parameter for use in a water electrolyzer. Finally, as a proof of concept, we have integrated the solar cells with the fabricated CMS/Ni water electrolyzer for energy efficient production of hydrogen fuel as shown in Fig. 6(E). Here, three solar cells were connected in parallel to drive the CMS/Ni water electrolyzer, which results in the splitting of water into hydrogen and oxygen gas bubbles as evident from the digital photograph given in Fig. 6(E) and Video S1 (ESI†). These studies suggested the use of non-precious CMS/Ni electrocatalysts for effective water splitting using solar energy, which is one of the cost-effective methods for the large-scale production of hydrogen in real life.

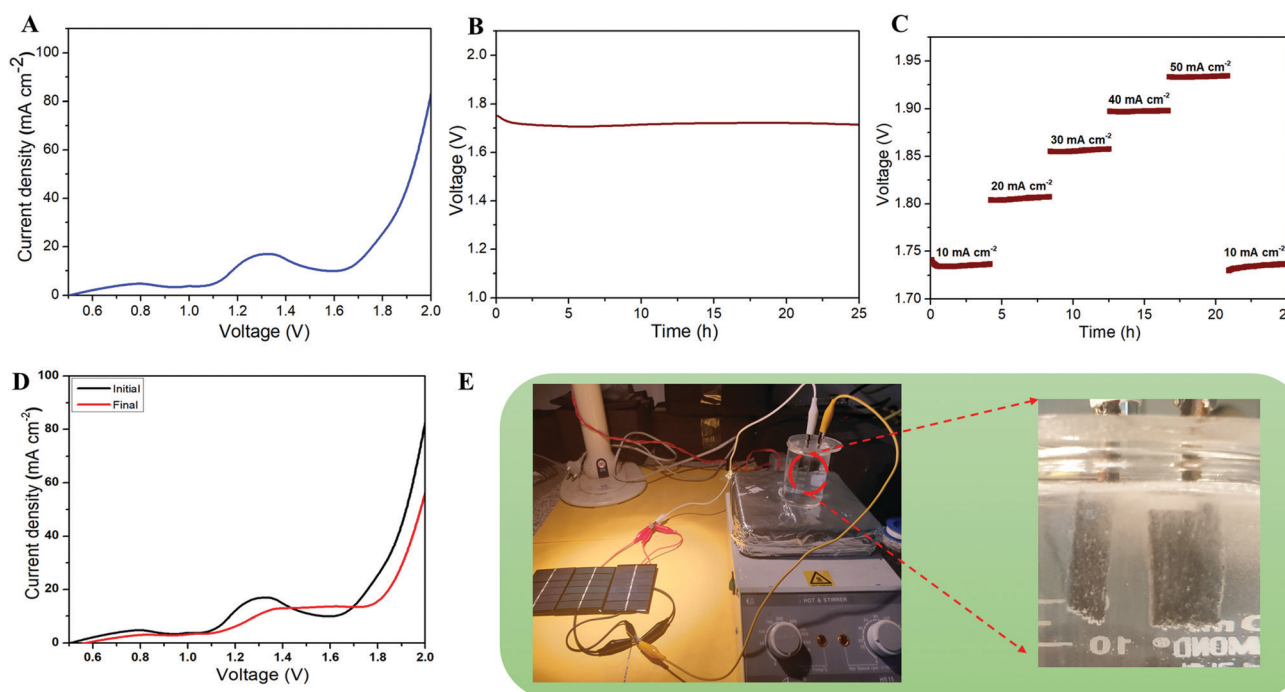


**Fig. 6** Electrochemical characterization of the CMS/Ni electrolyzer in 1 M KOH. (A) LSVs (scan rate of  $10 \text{ mV s}^{-1}$ ). (B) Chronopotentiometry durability test (without iR-compensated) at a constant current of  $50 \text{ mA cm}^{-2}$ . (C) Chronopotentiometry durability test with different applied currents. (D) Comparative plot of LSV analysis. (E) Practical application demonstrating the solar cell driven CMS/Ni electrolyzer depicting the formation of O<sub>2</sub> and H<sub>2</sub> gas bubbles, respectively.

## 4. Conclusion

In conclusion, a cost-effective CMS/Ni foam electrocatalyst was developed and explored as a bifunctional electrocatalyst for electrochemical water splitting. The binder free CMS/Ni electrocatalyst exhibit excellent electrochemical HER and OER with low overpotential values of 213 mV and 350 mV with a low Tafel slope and excellent electrochemical stability. A water electrolyzer fabricated using a CMS/Ni electrocatalyst (as both the anode and cathode) showed that a very low voltage of 1.62 V is required to attain 50 mA cm<sup>-2</sup>. Here, we have also successfully demonstrated the real time application of electrochemical water splitting driven by solar energy using the fabricated CMS/Ni electrocatalyst. These experimental strategies might give new inspiration for the researchers to focus on ternary transition metal chalcogenides in alkaline medium, which will accelerate the research into the field of clean and cost-effective electrocatalysis.

## Conflicts of interest

There are no conflicts to declare.

## Acknowledgements

This work was supported by the Basic Science Research Program through the National Research Foundation of Korea (NRF) grant funded by the Korean government (MSIT) (2018R1A4A1025998, 2019R1A2C3009747, and 2020R1A2C2007366).

## References

- 1 Z. W. She, J. Kibsgaard, C. F. Dickens, I. Chorkendorff, J. K. Nørskov and T. F. Jaramillo, *Science*, 2017, **355**, 6321, DOI: 10.1126/science.eaad4998.
- 2 J. Zhu, L. Hu, P. Zhao, L. Y. S. Lee and K. Y. Wong, *Chem. Rev.*, 2020, **120**, 851–918.
- 3 M. R. Palacín, *Chem. Soc. Rev.*, 2009, **38**, 2565–2575.
- 4 J. Suntivich, H. A. Gasteiger, N. Yabuuchi, H. Nakanishi, J. B. Goodenough and Y. Shao-Horn, *Nat. Chem.*, 2011, **3**, 546–550.
- 5 N. T. Suen, S. F. Hung, Q. Quan, N. Zhang, Y. J. Xu and H. M. Chen, *Chem. Soc. Rev.*, 2017, **46**, 337–365.
- 6 H. Ahmad, S. K. Kamarudin, L. J. Minggu and M. Kassim, *Renewable Sustainable Energy Rev.*, 2015, **43**, 599–610.
- 7 D. C. Nguyen, D. T. Tran, T. L. L. Doan, D. H. Kim, N. H. Kim and J. H. Lee, *Adv. Energy Mater.*, 2020, **10**, 1903289.
- 8 B. Y. Guan, S. L. Zhang and X. W. D. Lou, *Angew. Chem., Int. Ed.*, 2018, **57**, 6176–6180.
- 9 J. N. Tiwari, N. K. Dang, S. Sultan, P. Thangavel, H. Y. Jeong and K. S. Kim, *Nat. Sustainability*, 2020, **3**, 556–563.
- 10 T. F. Jaramillo, K. P. Jørgensen, J. Bonde, J. H. Nielsen, S. Horch and I. Chorkendorff, *Science*, 2007, **317**, 100–102.
- 11 I. Roger, M. A. Shipman and M. D. Symes, *Nat. Rev. Chem.*, 2017, **1**, 0003.
- 12 J. Zheng, W. Sheng, Z. Zhuang, B. Xu and Y. Yan, *Sci. Adv.*, 2016, **2**, 1–9.
- 13 V. Pfeifer, T. E. Jones, J. J. Velasco Vélez, C. Massué, M. T. Greiner, R. Arrigo, D. Teschner, F. Girgsdies, M. Scherzer, J. Allan, M. Hashagen, G. Weinberg, S. Piccinin, M. Hävecker, A. Knop-Gericke and R. Schlögl, *Phys. Chem. Chem. Phys.*, 2016, **18**, 2292–2296.
- 14 Y. Peng, K. Jiang, W. Hill, Z. Lu, H. Yao and H. Wang, *ACS Appl. Mater. Interfaces*, 2019, **11**, 3971–3977.
- 15 S. Siracusano, N. Hodnik, P. Jovanovic, F. Ruiz-Zepeda, M. Šala, V. Baglio and A. S. Aricò, *Nano Energy*, 2017, **40**, 618–632.
- 16 S. Chandrasekaran, L. Yao, L. Deng, C. Bowen, Y. Zhang, S. Chen, Z. Lin, F. Peng and P. Zhang, *Chem. Soc. Rev.*, 2019, **48**, 4178–4280.
- 17 J. Yin, J. Jin, H. Lin, Z. Yin, J. Li, M. Lu, L. Guo, P. Xi, Y. Tang and C. H. Yan, *Adv. Sci.*, 2020, **7**, 1903070.
- 18 S. Anantharaj, S. R. Ede, K. Sakthikumar, K. Karthick, S. Mishra and S. Kundu, *ACS Catal.*, 2016, **6**, 8069–8097.
- 19 J. Joo, T. Kim, J. Lee, S. Il Choi and K. Lee, *Adv. Mater.*, 2019, **31**, 1–23.
- 20 G. Fu and J. M. Lee, *J. Mater. Chem. A*, 2019, **7**, 9386–9405.
- 21 P. Zhang, X. F. Lu, J. Nai, S. Zang and X. W. (David) Lou, *Adv. Sci.*, 2019, **6**, 1900576.
- 22 H. Xu, S. Ci, Y. Ding, G. Wang and Z. Wen, *J. Mater. Chem. A*, 2019, **7**, 8006–8029.
- 23 W. Liu, J. Bao, M. Guan, Y. Zhao, J. Lian, J. Qiu, L. Xu, Y. Huang, J. Qian and H. Li, *Dalton Trans.*, 2017, **46**, 8372–8376.
- 24 Y. Yan, B. Y. Xia, B. Zhao and X. Wang, *J. Mater. Chem. A*, 2016, **4**, 17587–17603.
- 25 H. Zhu, J. Zhang, R. Yanzhang, M. Du, Q. Wang, G. Gao, J. Wu, G. Wu, M. Zhang, B. Liu, J. Yao and X. Zhang, *Adv. Mater.*, 2015, **27**, 4752–4759.
- 26 D. Wang, X. Zhang, Z. Du, Z. Mo, Y. Wu, Q. Yang, Y. Zhang and Z. Wu, *Int. J. Hydrogen Energy*, 2017, **42**, 3043–3050.
- 27 I. S. Amiin, Z. Pu, X. Liu, K. A. Owusu, H. G. R. Monestel, F. O. Boakye, H. Zhang and S. Mu, *Adv. Funct. Mater.*, 2017, **27**, 1702300.
- 28 W. Chen, H. Chen, H. Zhu, Q. Gao, J. Luo, Y. Wang, S. Zhang, K. Zhang, C. Wang, Y. Xiong, Y. Wu, X. Zheng, W. Chu, L. Song and Z. Wu, *Small*, 2014, **10**, 4637–4644.
- 29 K. Zhang, Y. Lin, C. Wang, B. Yang, S. Chen, S. Yang, W. Xu, H. Chen, W. Gan, Q. Fang, G. Zhang, G. Li and L. Song, *J. Phys. Chem. C*, 2016, **120**, 13120–13125.
- 30 P. D. Tran, M. Nguyen, S. S. Pramana, A. Bhattacharjee, S. Y. Chiam, J. Fize, M. J. Field, V. Artero, L. H. Wong, J. Loo and J. Barber, *Energy Environ. Sci.*, 2012, **5**, 8912–8916.
- 31 D. Y. W. Yu, R. L. Lee, R. Yi, S. Y. Chiam and P. D. Tran, *Electrochim. Acta*, 2014, **115**, 337–343.
- 32 S. Sahoo, K. Krishnamoorthy, P. Pazhamalai and S. J. Kim, *Nanoscale*, 2018, **10**, 13883–13888.
- 33 V. K. Mariappan, K. Krishnamoorthy, P. Pazhamalai, S. Sahoo, S. S. Nardekar and S.-J. J. Kim, *Nano Energy*, 2019, **57**, 307–316.
- 34 P. Thangavel, M. Ha, S. Kumaraguru, A. Meena, A. N. Singh, A. M. Harzandi and K. S. Kim, *Energy Environ. Sci.*, 2020, **13**, 3447–3458.
- 35 C. C. L. McCrory, S. Jung, I. M. Ferrer, S. M. Chatman, J. C. Peters and T. F. Jaramillo, *J. Am. Chem. Soc.*, 2015, **137**, 4347–4357.





- 36 H. Yuan, S. Wang, X. Gu, B. Tang, J. Li and X. Wang, *J. Mater. Chem. A*, 2019, **7**, 19554–19564.
- 37 J. Zhou, G. Xu, Z. Zhang and H. Wang, *New J. Chem.*, 2019, **43**, 9574–9582.
- 38 A. Sivanantham, P. Ganesan and S. Shanmugam, *Adv. Funct. Mater.*, 2016, **26**, 4661–4672.
- 39 S. Shit, S. Chhetri, W. Jang, N. C. Murmu, H. Koo, P. Samanta and T. Kuila, *ACS Appl. Mater. Interfaces*, 2018, **10**, 27712–27722.
- 40 A. Irshad and N. Munichandraiah, *ACS Appl. Mater. Interfaces*, 2017, **9**, 19746–19755.
- 41 X. Ma, W. Zhang, Y. Deng, C. Zhong, W. Hu and X. Han, *Nanoscale*, 2018, **10**, 4816–4824.
- 42 A. Sivanantham and S. Shanmugam, *Appl. Catal., B*, 2017, **203**, 485–493.
- 43 P. Cheng, C. Yuan, Q. Zhou, X. Hu, J. Li, X. Lin, X. Wang, M. Jin, L. Shui, X. Gao, R. Nötzel, G. Zhou, Z. Zhang and J. Liu, *J. Phys. Chem. C*, 2019, **123**, 5833–5839.
- 44 A. Shankar, R. Elakkiya and G. Maduraiveeran, *New J. Chem.*, 2020, **44**, 5071–5078.
- 45 K. S. Bhat and H. S. Nagaraja, *ChemistrySelect*, 2020, **5**, 2455–2464.
- 46 S. Anantharaj, S. R. Ede, K. Karthick, S. Sam Sankar, K. Sangeetha, P. E. Karthik and S. Kundu, *Energy Environ. Sci.*, 2018, **11**, 744–771.
- 47 K. Krishnamoorthy, P. Pazhamalai, V. K. Mariappan, S. S. Nardekar, S. Sahoo and S.-J. Kim, *Nat. Commun.*, 2020, **11**, 2351.
- 48 D. Liu, Q. Lu, Y. Luo, X. Sun and A. M. Asiri, *Nanoscale*, 2015, **7**, 15122–15126.
- 49 W. Dai, K. Ren, Y. an Zhu, Y. Pan, J. Yu and T. Lu, *J. Alloys Compd.*, 2020, **844**, 156252.
- 50 J. Bai, T. Meng, D. Guo, S. Wang, B. Mao and M. Cao, *ACS Appl. Mater. Interfaces*, 2018, **10**, 1678–1689.
- 51 S. Sahoo, K. Krishnamoorthy, P. Pazhamalai, V. K. Mariappan and S. J. Kim, *Int. J. Hydrogen Energy*, 2018, **43**, 12222–12232.

